Supplementary Information: Net-Negative Carbon Valorization in Wastewater Treatment via Sequential Thermochemical-Electrochemical Coupling

Xiangyu Zheng[1#], Menglan Xiao[2#], Jianming Zhu[1], Xin Li[1], Jundong Wang[1], Pan Zhu[1], Meiping Tong[1*], Zishuai Zhang[1,3*]

[1]The Key Laboratory of Water and Sediment Sciences, Ministry of Education, College of Environmental Science and Engineering, Peking University, Beijing, 100871, China

[2] Flavors and Fragrance Engineering & Technology Research Center of Henan Province, College of Tobacco Science, Henan Agricultural University, Zhengzhou, Henan 450002, China

[3]Institute of Carbon Neutrality, Peking University, Beijing 100871, China

This file includes:

Supplementary Note 1: Life Cycle Assessment (LCA)

1.1 System boundary and functional unit

The life cycle assessment (LCA) covers 32 Waste-to-Chemical (WtC) pathways that integrate thermochemical (T) and electrochemical (E) processes in sequential or parallel architectures. The system boundary includes fugitive CH_4 and CO_2 emissions from wastewater treatment plants (WWTPs), their conversion into C_1 and C_2 products-formate, methanol (MeOH), acetate, and ethanol (EtOH)-as well as the associated energy and material inputs required for gas capture and conversion. These products were selected due to their compatibility with WWTP operations, particularly as external carbon sources that can be reused in situ to replace conventional chemicals for denitrification. Under alkaline wastewater-treatment conditions, formate and acetate represent the dominant product forms and can be directly reused without additional downstream conversion or neutralization. In contrast, gaseous products (e.g., CO and syngas) were excluded, as they are not directly applicable within WWTP processes and would require additional separation, storage, and downstream utilization beyond the defined system boundary. Details are provided in Supplementary Note 1.

Displacement credits are assigned when the produced chemicals substitute conventional production routes or are reused within WWTP processes. Both direct process emissions and avoided emissions are included in the LCA framework. The primary functional unit is defined as the treatment of 1 m^3 of wastewater, ensuring that all results are normalized to the service provided at the plant scale. As a sensitivity analysis, results were also normalized to 1 kg CO_2-equivalent of avoided emissions to reflect a climate mitigation perspective. Both functional units yielded consistent relative rankings of the WtC pathways, indicating the robustness of the conclusions. Sequential configurations are denoted by "-", whereas parallel configurations are denoted by "/". In sequential pathways, CH_4 is first converted to CO_2, followed by subsequent conversion of CO_2 into the target product. In parallel pathways, CH_4 and CO_2 are independently converted into the same product through separate branches. Each configuration is evaluated for four target products (formate, MeOH, acetate, and EtOH), resulting in a total of 32 pathways (Table S1).

Table S1. Overview of the Waste-to-Chemical (WtC) pathways considered in this study

Architecture	Process	CH_4 process (step,1)	CO_2 process (step,2)	Products*
Sequential	T-T	$CH_4+2O_2\rightarrow CO_2+2H_2O$	$CO_2+H_2\rightarrow HCOOH$	formate
Sequential	T-E	$CH_4+2O_2\rightarrow CO_2+2H_2O$	$CO_2+H_2O\rightarrow HCOOH+0.5O_2$	formate
Sequential	E-T	$CH_4+2O_2\rightarrow CO_2+2H_2O$	$CO_2+H_2\rightarrow HCOOH$	formate
Sequential	E-E	$CH_4+2O_2\rightarrow CO_2+2H_2O$	$CO_2+H_2O\rightarrow HCOOH+0.5O_2$	formate
Parallel	T/T	$CH_4+1.5O_2\rightarrow HCOOH+H_2O$	$CO_2+H_2\rightarrow HCOOH$	formate
Parallel	T/E	$CH_4+1.5O_2\rightarrow HCOOH+H_2O$	$CO_2+H_2O\rightarrow HCOOH+0.5O_2$	formate
Parallel	E/T	$CH_4+1.5O_2\rightarrow HCOOH+H_2O$	$CO_2+H_2\rightarrow HCOOH$	formate
Parallel	E/E	$CH_4+1.5O_2\rightarrow HCOOH+H_2O$	$CO_2+H_2O\rightarrow HCOOH+0.5O_2$	formate
Sequential	T-T	$CH_4+2O_2\rightarrow CO_2+2H_2O$	$CO_2+3H_2\rightarrow CH_3OH+H_2O$	MeOH
Sequential	T-E	$CH_4+2O_2\rightarrow CO_2+2H_2O$	$CO_2+2H_2O\rightarrow CH_3OH+1.5O_2$	MeOH
Sequential	E-T	$CH_4+2O_2\rightarrow CO_2+2H_2O$	$CO_2+3H_2\rightarrow CH_3OH+H_2O$	MeOH
Sequential	E-E	$CH_4+2O_2\rightarrow CO_2+2H_2O$	$CO_2+2H_2O\rightarrow CH_3OH+1.5O_2$	MeOH
Parallel	T/T	$CH_4+0.5O_2\rightarrow CH_3OH$	$CO_2+3H_2\rightarrow CH_3OH+H_2O$	MeOH
Parallel	T/E	$CH_4+0.5O_2\rightarrow CH_3OH$	$CO_2+2H_2O\rightarrow CH_3OH+1.5O_2$	MeOH
Parallel	E/T	$CH_4+0.5O_2\rightarrow CH_3OH$	$CO_2+3H_2\rightarrow CH_3OH+H_2O$	MeOH
Parallel	E/E	$CH_4+0.5O_2\rightarrow CH_3OH$	$CO_2+2H_2O\rightarrow CH_3OH+1.5O_2$	MeOH
Sequential	T-T	$CH_4+2O_2\rightarrow CO_2+2H_2O$	$2CO_2+4H_2\rightarrow CH_3COOH+2H_2O$	acetate
Sequential	T-E	$CH_4+2O_2\rightarrow CO_2+2H_2O$	$2CO_2+2H_2O\rightarrow CH_3COOH+2O_2$	acetate
Sequential	E-T	$CH_4+2O_2\rightarrow CO_2+2H_2O$	$2CO_2+4H_2\rightarrow CH_3COOH+2H_2O$	acetate
Sequential	E-E	$CH_4+2O_2\rightarrow CO_2+2H_2O$	$2CO_2+2H_2O\rightarrow CH_3COOH+2O_2$	acetate
Parallel	T/T	$2CH_4+2O_2\rightarrow CH_3COOH+2H_2O$	$2CO_2+4H_2\rightarrow CH_3COOH+2H_2O$	acetate
Parallel	T/E	$2CH_4+2O_2\rightarrow CH_3COOH+2H_2O$	$2CO_2+2H_2O\rightarrow CH_3COOH+2O_2$	acetate
Parallel	E/T	$2CH_4+2O_2\rightarrow CH_3COOH+2H_2O$	$2CO_2+4H_2\rightarrow CH_3COOH+2H_2O$	acetate
Parallel	E/E	$2CH_4+2O_2\rightarrow CH_3COOH+2H_2O$	$2CO_2+2H_2O\rightarrow CH_3COOH+2O_2$	acetate
Sequential	T-T	$CH_4+2O_2\rightarrow CO_2+2H_2O$	$2CO_2+6H_2\rightarrow C_2H_5OH+3H_2O$	EtOH
Sequential	T-E	$CH_4+2O_2\rightarrow CO_2+2H_2O$	$2CO_2+3H_2O\rightarrow C_2H_5OH+3O_2$	EtOH
Sequential	E-T	$CH_4+2O_2\rightarrow CO_2+2H_2O$	$2CO_2+6H_2\rightarrow C_2H_5OH+3H_2O$	EtOH
Sequential	E-E	$CH_4+2O_2\rightarrow CO_2+2H_2O$	$2CO_2+3H_2O\rightarrow C_2H_5OH+3O_2$	EtOH
Parallel	T/T	$2CH_4+O_2\rightarrow C_2H_5OH+H_2O$	$2CO_2+6H_2\rightarrow C_2H_5OH+3H_2O$	EtOH
Parallel	T/E	$2CH_4+O_2\rightarrow C_2H_5OH+H_2O$	$2CO_2+3H_2O\rightarrow C_2H_5OH+3O_2$	EtOH
Parallel	E/T	$2CH_4+O_2\rightarrow C_2H_5OH+H_2O$	$2CO_2+6H_2\rightarrow C_2H_5OH+3H_2O$	EtOH
Parallel	E/E	$2CH_4+O_2\rightarrow C_2H_5OH+H_2O$	$2CO_2+3H_2O\rightarrow C_2H_5OH+3O_2$	EtOH

*Formic-acid- and acetic-acid-derived products are represented as formate and acetate, respectively, after KOH addition for direct reuse as external carbon sources under alkaline wastewater-treatment conditions.

1.2 Calculation of carbon emissions

Across all 32 WtC pathways (Table S1), total carbon emissions ($Emission_{total}$) were calculated by summing baseline wastewater treatment emissions and the energy and material requirements of capture and conversion processes, while subtracting avoided emissions from captured CH_4/CO_2 and substituted chemical products. The general calculation framework is given in Equation (1), all values are reported per m^3 of wastewater treated unless otherwise specified.

$$Emission_{total} = Emission_{WWTP} + Emission_{capture} + Emission_{energy} + Emission_{material} - Emission_{avoided} - Emission_{credits} \quad \text{(Eq. S1)}$$

where $Emission_{total}$ represents total carbon emission (kg CO_2e m^{-3} wastewater treated), $Emission_{WWTP}$ represents baseline wastewater treatment emissions (kg CO_2e m^{-3}, Table S2), $Emission_{capture}$ represents emission from CH_4 and CO_2 capture (kg CO_2e m^{-3}, see Section 1.2.1), $Emission_{energy}$ represents emissions associated with energy consumption (kg CO_2e m^{-3}, see Section 1.2.2), $Emission_{material}$ represents carbon emission from material consumption (kg CO_2e m^{-3}, see Section 1.2.3), $Emission_{avoided}$ refers to avoided emissions from preventing direct release CH_4 and CO_2 (kg CO_2e m^{-3}, see Section 1.2.4), $Emission_{credits}$ represents substitution credits from replacing conventional chemical production (kg CO_2e m^{-3}, see Section 1.2.5). All values are reported per m^3 of wastewater treated unless otherwise specified.

Table S2. Carbon emissions and fugitive carbon emissions from wastewater treatment in China[1]

Category		Unit	Amount
Total carbon emission		kg CO_2e m^{-3}	0.7917
Indirect carbon emission	Chemicals	kg CO_2e m^{-3}	0.1112
	Electricity	kg CO_2e m^{-3}	0.3303
Fugitive gas emission		kg CO_2e m^{-3}	0.3502
	CH_4	kg CH_4 m^{-3}	0.0081
	CO_2 (fossil)	kg CO_2e m^{-3}	0.0093
	CO_2 (all)	kg CO_2e m^{-3}	0.0929

1.2.1 Emissions from CH_4/CO_2 capture ($Emission_{capture}$)

The emissions from CH_4/CO_2 capture were calculated as:

$$Emission_{capture} = E_{capture} \times EF_{grid} \quad \text{(Eq. S2)}$$

where $E_{capture}$ is the electricity consumption for gas separation normalized to the functional unit (kWh m^{-3} wastewater, Table S3), and EF_{grid} is the regional grid emission factor (kg CO_2e kWh^{-1}), taken as 0.537 kg CO_2e kWh^{-1} based on the national average (Table S12).

Methane concentration, capture efficiency, and energy consumption were adopted from literature-reported values for wastewater treatment biogas systems. Raw biogas typically contains 50-70% CH_4, and pressure swing adsorption (PSA) systems achieve methane recovery efficiencies of 85-98%. The associated energy consumption for both CH_4 upgrading and industrial CO_2 capture is typically reported in the range of 0.1-0.3 kWh Nm^{-3}. In this study, representative values of 0.185 kWh Nm^{-3} and 72.6 kJ mol^{-1} (equivalent to 0.2 kWh Nm^{-3}) were adopted in this study, consistent with the typical range reported in the literature[2-7].

All energy consumption values reported on a volumetric gas basis (kWh Nm^{-3}) were converted to the functional unit (kWh m^{-3} wastewater treated) based on the stoichiometrically derived gas amounts. Gas quantities were obtained from mass-based results (Table S2) and converted to molar quantities to ensure consistency with reaction stoichiometry (Table S3).

Table S3. Energy consumption for CH_4 and CO_2 capture and its conversion to the functional unit basis

Category	Volumetric gas basis ($kWh\ Nm^{-3}$)	Converted to $kWh\ mol^{-1}$	n ($mol\ m^{-3}$ wastewater)	Energy consumption ($kWh\ m^{-3}$ wastewater)
CH_4	0.185[2]	0.0044	0.507	0.0022
CO_2	0.200[3]	0.0202	2.110	0.0426

Note: The volumetric energy consumption for CH_4 capture (0.185 $kWh\ Nm^{-3}$) and CO_2 capture (0.200 $kWh\ Nm^{-3}$) were adapted from Bauer et al. (2013)[2] and He and Hägg (2014)[3], respectively. The remaining values were calculated by converting the volumetric energy consumption to a molar basis and subsequently normalizing it to the functional unit used in this study.

1.2.2 Emissions from energy consumption ($Emission_{energy}$)

The GHG emissions from energy consumption processes were calculated as:

$$Emission_{energy} = E_{total} \times EF_{grid} \quad \text{(Eq. S3)}$$

$$E_{total} = E_{step,1} + E_{step,2} + E_{aux} \quad \text{(Eq. S4)}$$

where $E_{step,1}$ and $E_{step,2}$ are the energy consumption of the first and second conversion steps, respectively, which may correspond to thermochemical and/or electrochemical processes depending on the WtC configuration (**Supplementary Fig. 1**). E_T and E_E denote the thermochemical and electrochemical energy consumption, respectively, and E_{aux} represents auxiliary energy consumption associated with supporting units. The total energy consumption is given by E_{total}. EF_{grid} is the regional grid emission factor (kg CO_2e kWh^{-1}), taken as 0.537 kg CO_2e kWh^{-1} based on the national average (Table S12).

For thermochemical processes, E_T was calculated based on energy consumption obtained from Aspen Plus simulations (Fig. S1). The total energy demand of all relevant unit operations was extracted from Aspen as the molar amount of target product (kWh mol^{-1}), and the corresponding GHG emissions were then obtained using Equation (5).

$$E_T = \frac{E_{comp} + E_{heat} + E_{reactor} + E_{separation}}{3600} \quad \text{(Eq. S5)}$$

where E_{comp}, E_{heat}, $E_{reactor}$, and $E_{separation}$ are the energy consumption of compression, heating, reaction, and separation processes (kJ mol^{-1}), respectively, obtained from Aspen Plus simulations, the factor 3600 is used to convert energy from kJ to kWh.

The energy consumption of thermochemical processes under different operating conditions is summarized in Table S4. The operating conditions (temperature, pressure, and conversion levels) used in the Aspen simulations were selected based on literature-reported ranges for thermochemical CO_2 and CH_4 conversion processes. For CO_2 hydrogenation, typical conditions of 200-400 °C and 10-50 bar were adopted[4-7], with single-pass conversions of 10-30% under recycle configurations[4]. For methane conversion, high-temperature processes operating at 700-1000 °C with high conversion efficiencies were considered[7]. These values represent typical operating ranges rather than optimized conditions.

Energy consumption values were obtained from Aspen Plus simulations by summing the energy demand of all major unit operations (Equation 5) and subsequently converted to GHG intensity using the grid emission factor. A recycle ratio was applied for CO_2 conversion processes to account for incomplete single-pass conversion. In contrast, CH_4 conversion processes were modeled without recycle, as the inclusion of recycle streams would substantially increase gas handling and compression energy due to the presence of inert components (e.g., N_2 in air), without providing additional benefits under high-conversion conditions. As a result, thermochemical efficiency differs from single-pass conversion for CO_2 processes with recycle, but approximates single-pass conversion for CH_4 processes without recycle (Table S5).

For electrochemical processes, E_E was calculated based on Equation (6):

$$E_E = \frac{n \times F \times U_{cell}}{3600 \times 1000 \times FE} \quad \text{(Eq. S6)}$$

where n is the number of electrons transferred per mole of product, F is the Faraday constant (96485 C mol^{-1}), U_{cell} is the applied cell potential (V), and FE is the Faradaic efficiency (Table S6). The factor 3600×1000 converts energy from J mol^{-1} to kWh mol^{-1}. From a thermodynamic perspective, the minimum energy requirement is defined by the Gibbs free energy change ($\Delta G = -nFE^0$), and the calculated energy values remain above this limit.

The electrochemical parameters (cell voltage and Faradaic efficiency) listed in Table S6 were selected based on a comprehensive survey of the literature. Reported values for each product pathway vary considerably depending on catalyst type, reactor configuration, and operating conditions. Therefore, ranges are provided to capture this variability, while the values in parentheses are adopted in this study as representative and moderately conservative operating conditions.

High Faradaic efficiencies (>90%) for formate production from CO_2 have been widely reported under comparable current densities and electrolyte conditions, whereas multi-carbon products generally exhibit lower efficiencies due to more complex reaction pathways. For CH_4 electrochemical conversion, reported efficiencies are typically lower, and the selected values reflect realistic experimental performance rather than idealized limits.

Auxiliary energy consumption includes minor energy inputs associated with pumping, mixing, and fluid transfer that are not explicitly accounted for in the main conversion processes. Energy-intensive operations such as gas separation, compression, and heat exchange are included in the primary energy terms ($E_{step,1}$ and $E_{step,2}$) and are therefore excluded here to avoid double counting.

The auxiliary energy consumption was calculated as Equation (7):

$$E_{aux} = P_{pump} \times t + \varphi_{mix} \times V_{tank} \times t \quad \text{(Eq. S7)}$$

where E_{aux} is the auxiliary energy consumption (kWh), P_{pump} is the pump power (kW), φ_{mix} is the mixing power density (kW m^{-3}), V_{tank} is the equivalent tank volume normalized to the functional unit (m^3), t is the operating time (h).

Representative values were adopted for auxiliary energy calculations based on typical wastewater treatment operations. A pump power of 0.1 kW and a mixing power density of 0.02 kW m^{-3} were assumed in this study. To ensure consistency with the functional unit of 1 m^3 wastewater treated, the tank volume was normalized to 1 m^3, with an operating time of 0.5 h. These values are consistent with reported ranges for pumping and mixing energy in wastewater treatment systems[8,9].

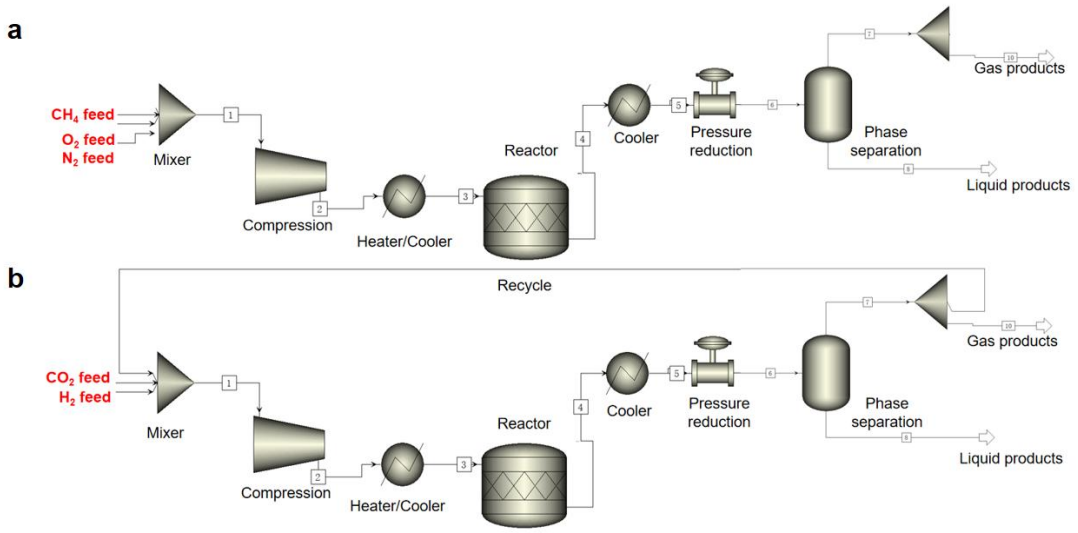

Supplementary Fig. 1. Aspen Plus simulation flowsheets of the thermochemical processes. a, CH_4 conversion to products (CO_2, formate, MeOH, acetate, and EtOH). **b**, CO_2 conversion to products (formate, MeOH, acetate, and EtOH).

Table S4. Aspen Plus simulation input parameters

Process	Temperature (℃)	Pressure (bar)	Single-pass conversion (%)	Recycle ratio
CO_2 → formate	250	25	20	0.95
CO_2 → MeOH	250	25	20	0.95
CO_2 → acetate	250	25	10	0.95
CO_2 → EtOH	250	25	10	0.95
CH_4 → CO_2	1000	1.01	95	0
CH_4 → formate	250	10	20	0
CH_4 → MeOH	350	10	20	0
CH_4 → acetate	300	10	20	0
CH_4 → EtOH	250	10	20	0

Thermochemical efficiency is calculated from Aspen Plus simulation outputs based on the molar flow rates of outlet products and their corresponding energy contents. In the LCA model, it is used as a lumped parameter to scale energy consumption, assuming that overall energy consumption scales inversely with thermochemical efficiency, ±10% variation in thermochemical efficiency is applied in the sensitivity analysis.

Table S5. Energy consumption of thermochemical processes based on Aspen Plus simulations

Process	CH_4 conversion (%)	CO_2 conversion (%)	Energy consumption from Aspen (kJ mol^{-1})
CO_2 → formate	81.49		505
CO_2 → MeOH	78.07		1406
CO_2 → acetate	40.95		1783
CO_2 → EtOH	39.69		2767
CH_4 → CO_2		95	1621
CH_4 → formate		20	766
CH_4 → MeOH		20	360
CH_4 → acetate		20	955
CH_4 → EtOH		20	641

Table S6. Electrochemical parameters used for energy estimation

Process	Transfer of electrons	Cell voltage (V)	*FE* (%)	References
CO_2 → formate	2	2.0-3.0 (2.5)	90-100 (95)	[10-19]
CO_2 → MeOH	6	2.0-2.8 (2.5)	40-60 (50)	[20-29]
CO_2 → acetate	8	2.0-2.7 (2.5)	40-60 (50)	[30-35]
CO_2 → EtOH	12	2.0-2.9 (2.5)	30-50 (40)	[36-38]
CH_4 → CO_2	8	1.7-2.5 (2.0)	80-90 (85)	/
CH_4 → formate	6	1.6-2.4 (2.0)	10-30 (20)	[39,40]
CH_4 → MeOH	2	1.5-2.3 (2.0)	10-30 (20)	[41,42]
CH_4 → acetate	8	1.0-2.6 (2.0)	10-30 (20)	[43]
CH_4 → EtOH	4	1.7-2.5 (2.0)	10-30 (20)	[43]

1.2.3 Emissions from material consumption of all reactions ($Emission_{material}$)

The GHG emissions from material consumption processes were calculated as:

$$Emission_{material} = \sum_{i} m_i \times EF_i \quad \text{(Eq. S8)}$$

$$m_i = n_i \times MW_i \quad \text{(Eq. S9)}$$

where m_i is the mass of material i consumed (kg per m^3 wastewater), n_i is the stoichiometric requirement of material i (mol, Tables S7-S10), MW_i is the molecular weight of material i (kg mol^{-1}), and EF_i is the emission factor of material i (kg CO_2e kg^{-1}, Table S11)[44,45].

Table S7. Stoichiometric material flows for formate production across sequential and parallel pathways

Process	CH_4 (mol)	CO_2 (mol)	H_2O (mol)	H_2 (mol)	O_2 (mol)	formate (mol)
T-T	0.507	2.592	0	2.592	0.964	2.074
T-E	0.507	2.592	2.592	0	0.964	2.463
E-T	0.507	2.567	0	2.567	0.964	1.769
E-E	0.507	2.567	2.567	0	0.964	2.101
T/T	0.507	2.110	0	2.110	0.722	1.790
T/E	0.507	2.110	2.110	0	0.722	1.790
E/T	0.507	2.110	0	2.110	0.722	0.524
E/E	0.507	2.110	2.110	0	0.722	0.524

Table S8. Stoichiometric material flows for MeOH production across sequential and parallel pathways

Process	CH_4 (mol)	CO_2 (mol)	H_2O (mol)	H_2 (mol)	O_2 (mol)	MeOH (mol)
T-T	0.507	2.592	0	7.777	0.964	2.074
T-E	0.507	2.592	5.185	0	0.964	1.296
E-T	0.507	2.567	0	7.701	0.964	2.054
E-E	0.507	2.567	5.134	0	0.964	1.283
T/T	0.507	2.110	0	6.331	0.241	1.790
T/E	0.507	2.110	4.221	0	0.241	1.790
E/T	0.507	2.110	0	6.331	0.241	1.157
E/E	0.507	2.110	4.221	0	0.241	1.157

Table S9. Stoichiometric material flows for acetate production across sequential and parallel pathways

Process	CH_4 (mol)	CO_2 (mol)	H_2O (mol)	H_2 (mol)	O_2 (mol)	acetate (mol)
T-T	0.507	2.592	0	5.185	0.964	1.037
T-E	0.507	2.592	2.592	0	0.964	1.296
E-T	0.507	2.567	0	5.134	0.964	1.027
E-E	0.507	2.567	2.567	0	0.964	1.283
T/T	0.507	2.110	0	4.221	0.482	0.895
T/E	0.507	2.110	2.110	0	0.482	0.946
E/T	0.507	2.110	0	4.221	0.482	1.106
E/E	0.507	2.110	2.110	0	0.482	1.157

Table S10. Stoichiometric material flows for EtOH production across sequential and parallel pathways

Process	CH_4 (mol)	CO_2 (mol)	H_2O (mol)	H_2 (mol)	O_2 (mol)	EtOH (mol)
T-T	0.507	2.592	0	7.777	0.964	1.037
T-E	0.507	2.592	3.888	0	0.964	1.037
E-T	0.507	2.567	0	7.701	0.964	1.027
E-E	0.507	2.567	3.851	0	0.964	1.027
T/T	0.507	2.110	0	6.331	0.482	0.895
T/E	0.507	2.110	3.166	0	0.482	0.946
E/T	0.507	2.110	0	6.331	0.482	0.895
E/E	0.507	2.110	3.166	0	0.482	0.946

CH_4 values represent the total feed amount, while only 95% of CH_4 was assumed to participate in reaction. The remaining unreacted methane was assumed to be vented and therefore not included in downstream stoichiometric conversion calculations. O_2 demand was therefore calculated based on the reacted CH_4 amount according to the stoichiometric ratio. Additional material consumption associated with product utilization was considered. In the porous solid electrolyte (PSE) reactor, the products are directly obtained as formate and acetate in an alkaline electrolyte, and therefore no additional external neutralization or pH adjustment is required.

Table S11. Carbon emission factors of input materials and product credits[44,45]

	Category	Amount	Unit
Input materials	Hydrogen	2.37	kg CO_2e kg^{-1}
	Oxygen	1.09	kg CO_2e kg^{-1}
	Water, deionised	0.00	kg CO_2e kg^{-1}
	KOH	0.80	kg CO_2e kg^{-1}
By-products	formate	3.64	kg CO_2e kg^{-1}
	MeOH	0.76	kg CO_2e kg^{-1}
	acetate	2.22	kg CO_2e kg^{-1}
	EtOH	0.49	kg CO_2e kg^{-1}

Note: Carbon emission factors of input materials were obtained from the ecoinvent database (v3)[44]. Product credits were calculated based on the avoided production of equivalent conventional chemicals using literature-derived life-cycle emission factors and IPCC AR6 guidance[45].

However, for consistency with conventional wastewater treatment practices and to ensure a comparable system boundary, stoichiometric amounts of KOH were included on an equivalent basis in the LCA/TEA framework. This treatment is used solely to account for the associated carbon footprint and economic cost of pH adjustment, rather than representing an actual process step in the PSE reactor. The associated KOH consumption was included in the material inventory and accounted for in both LCA and TEA calculations (Table S11). This approach ensures methodological consistency while preserving the practical advantage of the PSE reactor configuration, where products are obtained in a directly reusable alkaline form without additional downstream processing.

1.2.4 Avoided emissions from gas emission treatment ($Emission_{avoided}$)

The avoided emissions from gas emission treatment were calculated as Equation (10):

$$Emission_{avoided} = \sum_{i} n_i \times MW_i \times GWP_i \quad \text{(Eq. S10)}$$

where n_i is the amount of gas *i* avoided (mol), MW_i is its molecular weight (kg mol^{-1}) (listed in Tables S7-S10), GWP_i is its global warming potential (29.8 kg CO_2e kg^{-1} for CH_4 and 1.0 kg CO_2e kg^{-1} for CO_2).

1.2.5 Avoided emissions from by-products substitution ($Emission_{credits}$)

Formate, methanol (MeOH), acetate, and ethanol (EtOH) are considered as substitutable products and credited as by-products *j* (Equation (S11-S12)).

$$Emission_{credits} = m_j \times EF_j \quad \text{(Eq. S11)}$$

$$m_j = n_j \times MW_j \quad \text{(Eq. S12)}$$

where n_j is the amount of products *j* (mol, Tables S7-S10), m_j is the corresponding mass (kg m^{-3}), MW_j is the molecular weight (kg mol^{-1}) and EF_j is the emission factor of the substituted conventional product (kg CO_2e kg^{-1}, Table S11).

1.3 Carbon emission of different provinces

The carbon emission factors were obtained from the Ecoinvent 3.10 database and the China Products Carbon Footprint Factors Database[46], representing region-specific and industry-relevant values (Table S12).

All calculations follow Equations (S1-S12), with the emission factors updated to reflect different electricity scenarios. The electricity-related carbon emission factors for each province in China were obtained from the China Products Carbon Footprint Factors Database and are summarized in Table S13[46].

Table S12. Life-cycle carbon emission factors of different electricity sources[46]

	Category	Amount	Unit
Baseline	National average	0.5370	kg CO_2e kWh^{-1}
Fossil-based electricity	Coal	0.9440	kg CO_2e kWh^{-1}
	Fossil fuel	0.8330	kg CO_2e kWh^{-1}
	Natural gas	0.4790	kg CO_2e kWh^{-1}
Low-carbon electricity	Photovoltaic power	0.0550	kg CO_2e kWh^{-1}
	Biomass	0.0460	kg CO_2e kWh^{-1}
	Wind power	0.0340	kg CO_2e kWh^{-1}
	Hydropower	0.0140	kg CO_2e kWh^{-1}
	Nuclear	0.0070	kg CO_2e kWh^{-1}

Note: Carbon emission factors of different electricity sources were obtained from the China Products Carbon Footprint Factors Database (CCG, 2025)[46]. The national-average value was used as the baseline electricity scenario, whereas source-specific values were used to represent fossil-based and low-carbon electricity scenarios in the LCA.

Table S13. Grid emission factors and wastewater treatment volumes by province

Province	Region	Grid carbon emission factors (kg CO_2e kWh^{-1})	Sewage treatment volume (10^4 m^3 $year^{-1}$)
Xinjiang	Northwest China	0.6230	75842
Ningxia		0.6420	26467
Qinghai		0.1570	17553
Gansu		0.4770	44935
Shanxi		0.6560	120815
Yunnan	Southwest China	0.1070	102259
Guizhou		0.4990	72643
Sichuan		0.1400	216531
Chongqing		0.5230	130520
Hainan	South China	0.4180	33294
Guangxi		0.4040	121672
Guangdong		0.4400	780295
Hunan	Central China	0.4900	216352
Hubei		0.4360	248266
Henan		0.6060	202547
Shandong	East China	0.6410	345420
Jiangxi		0.5750	97724
Fujian		0.4090	128708
Anhui		0.6780	177204
Zhejiang		0.5150	318917
Jiangsu		0.5980	423201
Shanghai		0.5850	209388
Heilongjiang	Northeast China	0.5370	107352
Jilin		0.4930	124109
Liaoning		0.5630	282144
Neimenggu	North China	0.6850	67443
Shaanxi		0.7100	82816
Hebei		0.7250	176073
Tianjin		0.7040	104964
Beijing		0.5580	193356

For regional analysis, provinces were grouped into seven geographical regions in China, and the spatial distribution is illustrated in **Supplementary Fig. 2**. The inset map in Fig. S2 does not represent a magnified local area but is included to indicate the South China Sea Islands (e.g., the Nansha Islands) as part of the national territory.

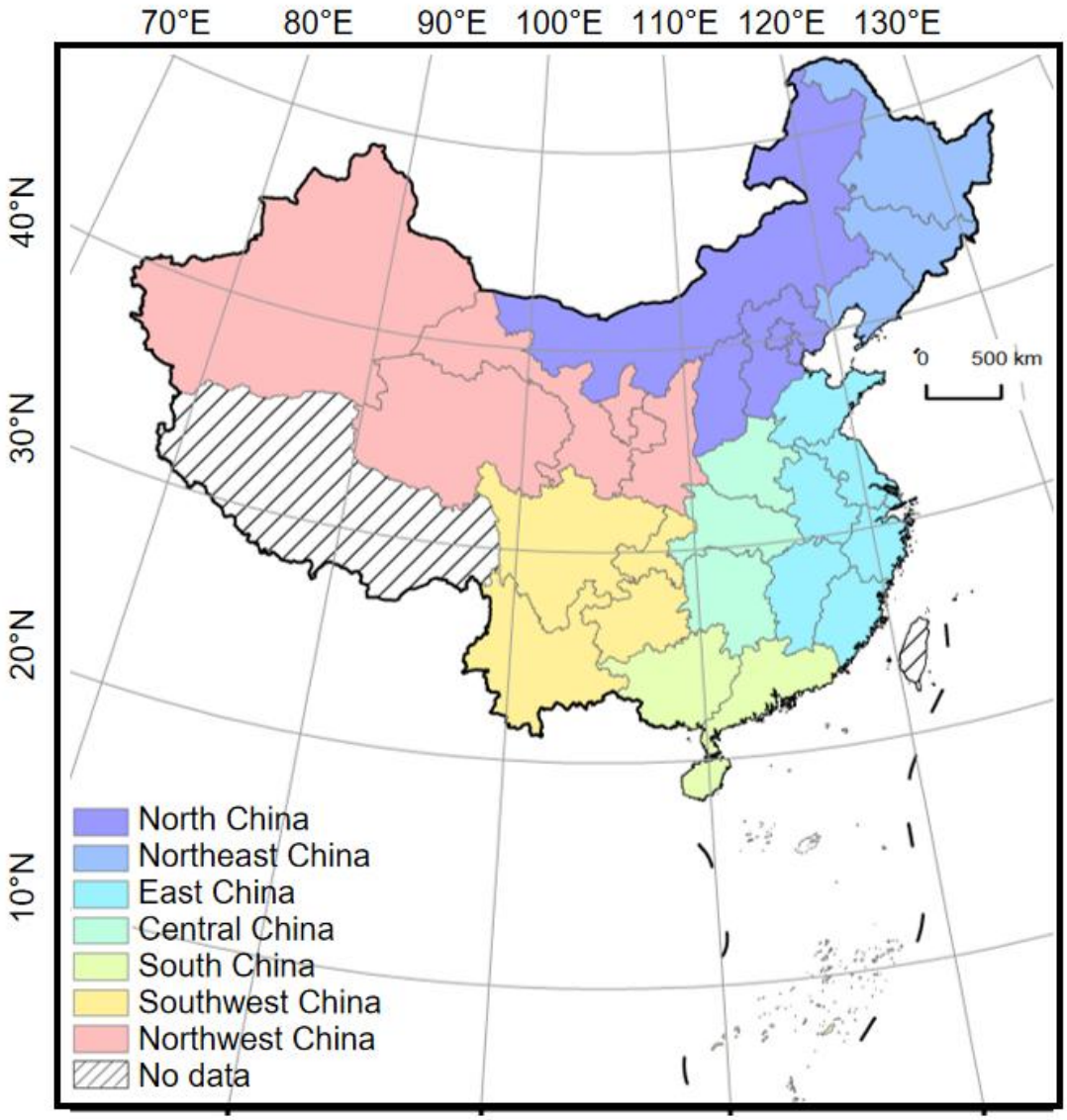

Supplementary Fig. 2. Regional classification of provinces in China. Provinces are grouped into seven geographical regions used in this study. Tibet is shown as No data, and Hong Kong, Macao, and Taiwan were not included in the regional analysis due to data unavailability.

1.4 Temporal modeling of GHG emissions

The temporal analysis was implemented as a scenario-based LCA, in which the same WtC pathways were evaluated under different time-specific background conditions (2009, 2019, 2030, and 2050), rather than as a dynamic simulation of process operation.

The temporal background inventories were adapted from Du et al. (2023)[1], who developed province-resolved wastewater-sector GHG scenarios for China under historical (2009 and 2019) and future (2030 and 2050) conditions. These inventories incorporate projected changes in wastewater treatment performance, electricity structure, chemical consumption, and wastewater-related fugitive emissions.

Specifically, the electricity structure and the corresponding grid emission factor (EF_{grid}, kg CO_2e kWh^{-1}) were treated as time-dependent background parameters, reflecting the projected decarbonization of the power sector (Table S14). Historical baseline values (2009) and current conditions (2019) were derived from reported data, whereas future scenarios (2030 and 2050) were constructed based on literature-informed projections of electricity mix and grid carbon intensity. The selected years represent historical baseline (2009), current conditions (2019), mid-term transition aligned with China's carbon peaking target (~2030), and long-term deep decarbonization (2050), respectively. These time-dependent EFgrid values were incorporated into Equation (3) to convert process electricity consumption into indirect GHG emissions. In addition, wastewater-related fugitive emissions, chemical consumption, and process energy demand were updated according to the corresponding temporal background inventories. Therefore, the temporal scenarios represent integrated background conditions rather than changes in a single parameter, allowing the combined influence of electricity decarbonization, wastewater emission profiles, and process-related inventories to be evaluated across different temporal scenarios.

Table S14 summarizes the evolution of grid emission factors and wastewater-related emissions under different temporal scenarios, which were used to define baseline and projected conditions for the temporal LCA analysis.

Table S14 China's carbon emissions and fugitive carbon emissions from WWTP in 2009, 2030, 2050[1]

Year			Amount	Unit
2009	Total carbon emission		0.6646	kg CO_2e m^{-3}
	Indirect carbon emission	Chemicals	0.0490	kg CO_2e m^{-3}
		Electricity	0.1943	kg CO_2e m^{-3}
	Fugitive carbon emission	CH_4	0.0103	kg m^{-3}
		N_2O	0.0004	kg m^{-3}
		CO_2 (fossil)	0.0116	kg m^{-3}
		CO_2 (all)	0.1161	kg m^{-3}
2030	Total carbon emission		0.8813	kg CO_2e m^{-3}
	Indirect carbon emission	Chemicals	0.0890	kg CO_2e m^{-3}
		Electricity	0.3408	kg CO_2e m^{-3}
	Fugitive carbon emission	CH_4	0.0106	kg m^{-3}
		N_2O	0.0005	kg m^{-3}
		CO_2 (fossil)	0.0091	kg m^{-3}
		CO_2 (all)	0.0910	kg m^{-3}
2050	Total carbon emission		0.7179	kg CO_2e m^{-3}
	Indirect carbon emission	Chemicals	0.0556	kg CO_2e m^{-3}
		Electricity	0.2107	kg CO_2e m^{-3}
	Fugitive carbon emission	CH_4	0.0106	kg m^{-3}
		N_2O	0.0005	kg m^{-3}
		CO_2 (fossil)	0.0091	kg m^{-3}
		CO_2 (all)	0.0910	kg m^{-3}

Note: Historical and projected wastewater-sector GHG inventories were adapted from Du et al. (2023)[1]. The temporal scenarios were implemented as integrated background inventories rather than by independently varying a single parameter. Accordingly, changes in wastewater-related fugitive emissions, electricity structure, chemical consumption, and process energy demand were incorporated simultaneously in the temporal LCA.

.

Supplementary Note 2: Techno-economic analysis (TEA)

2.1 Calculation of carbon emissions

A techno-economic analysis (TEA) was carried out to assess the economic feasibility of WtC pathways. The evaluation is based on the plant-gate levelized cost (US$ m^{-3} wastewater treated, hereafter expressed as US$ m^{-3}), which incorporates electricity costs, input chemicals, equipment construction, installation and maintenance, sewage treatment, and credits from obtained chemicals and carbon reductions. The calculation framework is given as in Equation 13:

$$C_{total} = C_{WWTP} + C_{electricity} + C_{chemical} + C_{equipment} - C_{product} - C_{carbon} \quad \text{(Eq. S13)}$$

where C_{total} is the plant-gate levelized cost (US$ m^{-3}), C_{WWTP} is the cost of sewage treatment, a value of 0.21 US$ m^{-3} was adopted based on the wastewater treatment pricing policy issued by the National Development and Reform Commission[47]. $C_{electricity}$ is the electricity cost (US$ m^{-3}), $C_{chemical}$ is the cost of input chemicals (US$ m^{-3}), $C_{equipment}$ is the cost of equipment construction, installation, and maintenance (US$ m^{-3}), $C_{product}$ is the revenue from chemical products (US$ m^{-3}), C_{carbon} is the revenue from carbon trading (US$ m^{-3}).

The electricity cost is calculated as:

$$C_{electricity} = p_{electricity} \times \left(E_{capture} + E_{total}\right) \quad \text{(Eq. S14)}$$

where $p_{electricity}$ is the average industrial electricity price in China (0.084 US$ kWh^{-1}), based on the National Development and Reform Commission[47]. $E_{capture}$ and E_{total} correspond to the energy terms defined in Table S3 and Equation (4), respectively.

The cost of input chemicals is calculated as:.

$$C_{chemical} = \sum_{i} m_i \times p_i \quad \text{(Eq. S15)}$$

where m_i is the consumption of chemical *i* (kg m^{-3} wastewater treated) and p_i is the unit market price of chemical *i* (US$ kg^{-1}). The chemicals considered include hydrogen, oxygen, and deionized water as well as potassium hydroxide (KOH) associated with product neutralization (Table S15). The prices of hydrogen, oxygen, deionized water, KOH, formate, methanol, acetate, and ethanol were obtained from the SCI99 Chemical Market Price Database[48], and represent typical values in China. KOH is included to account for the stoichiometric neutralization of acidic products (formate and acetate) into their corresponding salts prior to reuse as external carbon sources in wastewater treatment, consistent with the assumptions adopted in the LCA model (Section 1.2.3).

Equipment costs, including construction, installation, and maintenance, were estimated using a simplified engineering assumption, expressed as a fraction of operating costs, following common practice in early-stage techno-economic assessments[49]. The equipment cost is calculated as:

$$C_{Equipment} = \alpha \times \left(C_{electricity} + C_{chemical}\right) \quad \text{(Eq. S16)}$$

where α is the cost factor, assumed to be 0.01 based on literature and engineering practice[49].

Revenue from chemical products is calculated as:

$$C_{products} = \sum_{i} m_j \times p_j \quad \text{(Eq. S17)}$$

where m_j is the mass of product j (kg m^{-3} wastewater treated) and p_j is the corresponding market price (US$ kg^{-1}). Formate, methanol (MeOH), acetate, and ethanol (EtOH) were obtained from the SCI99 Chemical Market Price Database[48], and represent typical values in China (Table S15).

Revenue from chemical products is calculated as:

$$C_{Carbon} = \frac{p_{Carbon} \times (Emission_{avoided} + Emission_{credits})}{1000} \quad \text{(Eq. S18)}$$

where p_{Carbon} is the carbon price in the emission trading system (20 US$ t^{-1} CO_2e), and $Emission_{avoided}$ and $Emission_{credits}$ are defined in Equations (10) and (11), respectively. Carbon prices in China's emission trading system typically range from 2 to 30 US$ t^{-1} CO_2e) and are projected to increase to ~40 US$ t^{-1} CO_2e by 2030[49-53]. A representative value of 20 US$ t^{-1} CO_2e was adopted based on the State and Trends of Carbon Pricing report published by the World Bank[52].

Table S15. Market prices of input materials and products used in the TEA[48]

	Category	Price (CNY kg^{-1})	Price (US$ kg^{-1})
Input materials	Hydrogen	25.6	3.56
	Oxygen	0.41	0.056
	Water, deionised	0.50	0.069
	KOH	5.0	0.69
By-products	formate	3.50	0.49
	MeOH	2.35	0.33
	acetate	2.37	0.33
	EtOH	5.64	0.78

Note: Market prices were obtained from the SCI99 Chemical Market Price Database (2024), which was used as the primary data source for techno-economic calculations[48]. Values were converted from CNY to US$ using the exchange rate adopted in this study.

Supplementary Note 3: System-level performance and scenario analysis of WtC pathways

3.1 Comparison of WtC pathways

Across all 32 WtC pathways (Table S1), $Emission_{total}$ were calculated according to Equation (1). All results are reported per m^3 of wastewater treated unless otherwise specified. The overall performance of all pathways is summarized in Table S16, which reports energy consumption and GHG intensity for each configuration. Pathways are grouped by product and ordered by GHG intensity within each group to enable comparison across different target products.

Table S16. Energy consumption and GHG intensity of all WtC pathways

Products	Architecture	Process	Energy consumption ($kWh\ m^{-3}$)	GHG intensity ($kg\ CO_2e\ m^{-3}$)
formate	Sequential	T-E	0.6149	0.5088
	Sequential	T-T	0.5400	0.5507
	Sequential	E-E	0.6467	0.5588
	Sequential	E-T	0.5733	0.5999
	Parallel	T/T	0.2905	0.6430
	Parallel	T/E	1.0849	1.0696
	Parallel	E/T	1.4677	1.4925
	Parallel	E/E	2.2621	1.9191
MeOH	Parallel	T/T	0.7131	1.100
	Sequential	T-T	1.0592	1.116
	Sequential	E-T	1.0183	1.119
	Parallel	E/T	1.0718	1.315
	Sequential	E-E	1.4503	1.379
	Sequential	T-E	1.4998	1.380
	Parallel	T/E	1.3035	1.417
	Parallel	E/E	1.6622	1.632
acetate	Sequential	T-T	0.7629	0.9138
	Sequential	E-T	0.7278	0.9215
	Parallel	T/T	0.4638	0.9599
	Parallel	T/E	1.2663	1.3631
	Parallel	E/T	1.4030	1.4405
	Sequential	E-E	1.8590	1.5004
	Sequential	T-E	1.9167	1.5042
	Parallel	E/E	2.2056	1.8437
EtOH	Parallel	T/T	0.6901	1.1368
	Sequential	T-T	1.0463	1.1404
	Sequential	E-T	1.0057	1.1436
	Parallel	T/E	1.0891	1.3269
	Parallel	E/T	2.5863	2.1551
	Parallel	E/E	2.9853	2.3452
	Sequential	E-E	3.2895	2.3701
	Sequential	T-E	3.3757	2.3913

The economic performance of all WtC pathways was evaluated based on the plant-gate levelized cost. The overall cost of each pathway is summarized in Table S17. Pathways are grouped by product and ordered by cost within each product group. Detailed cost results for all configurations are provided in Table S17.

Table S17. Plant-gate levelized cost of all WtC pathways

Products	Architecture	Process	Plant-gate levelized cost (US$ m^{-3})
formate	Parallel	T/T	0.2119
	Sequential	T-E	0.2132
	Sequential	E-E	0.2179
	Sequential	T-T	0.2288
	Sequential	E-T	0.2331
	Parallel	T/E	0.2878
	Parallel	E/T	0.3446
	Parallel	E/E	0.4205
MeOH	Parallel	T/T	0.3082
	Parallel	E/T	0.3088
	Sequential	E-T	0.3428
	Sequential	E-E	0.3435
	Sequential	T-T	0.3469
	Sequential	T-E	0.3476
	Parallel	T/E	0.3647
	Parallel	E/E	0.3653
acetate	Parallel	T/T	0.2704
	Sequential	E-T	0.2968
	Sequential	T-T	0.3000
	Parallel	E/T	0.3274
	Parallel	T/E	0.3455
	Sequential	E-E	0.3655
	Sequential	T-E	0.3700
	Parallel	E/E	0.4025
EtOH	Parallel	T/T	0.2680
	Sequential	E-T	0.2969
	Sequential	T-T	0.3000
	Parallel	T/E	0.3033
	Parallel	E/T	0.4212
	Parallel	E/E	0.4564
	Sequential	E-E	0.4813
	Sequential	T-E	0.4882

To evaluate the influence of auxiliary energy and material inputs on the robustness of the LCA results, additional contributions associated with supporting units and product utilization were incorporated into the revised analysis. Representative WtC pathways were selected to compare the simplified model and the revised model including auxiliary inputs (Table S18).

Overall, the inclusion of auxiliary contributions resulted in only minor changes in the calculated energy consumption and GHG emissions. Across all representative pathways, the average deviation in total energy consumption was 5.94 ± 2.65%, while the corresponding deviation in GHG emissions was 2.65 ± 0.62%. Importantly, these differences did not alter the relative ranking of pathways or the main conclusions of this study. The results therefore indicate that the simplified framework provides a reasonable approximation for pathway-level

comparison, while the revised model further improves the completeness and consistency of the system boundary.

Table S18. Influence of auxiliary energy and material inputs on representative WtC pathways

Process	Energy without auxiliary inputs (kWh m^{-3})	Energy with auxiliary inputs (kWh m^{-3})	Deviation (%)	GHG without auxiliary inputs (kg CO_2e m^{-3})	GHG with auxiliary inputs (kg CO_2e m^{-3})	Deviation (%)
T/T	0.5080	0.5400	5.93%	0.5335	0.5507	3.12%
T-E	0.5829	0.6149	5.20%	0.4916	0.5088	3.38%
E-E	0.5413	0.5733	5.58%	0.5827	0.5999	2.86%
T-T	0.6147	0.6467	4.95%	0.5416	0.5588	3.08%
E-T	0.2585	0.2905	11.02%	0.6258	0.6430	2.67%
T/E	1.0529	1.0849	2.95%	1.0524	1.0696	1.61%
E/T	0.3195	0.3515	9.10%	0.5916	0.6088	2.82%
E/E	1.1139	1.1459	2.79%	1.0182	1.0354	1.66%

Sensitivity analysis was performed for the representative T-E pathway by varying key parameters by ±10% while keeping all other variables constant. All results are reported per m^3 of wastewater treated unless otherwise specified. The corresponding changes in energy consumption and GHG intensity are summarized in Table S18. The impact of each parameter was quantified as the percentage change in GHG intensity relative to the baseline case.

Among the parameters considered, Faradaic efficiency exhibited the largest influence on system performance, followed by formic acid credit and grid emission factor, while thermochemical CH_4 conversion and cell voltage showed comparatively smaller effects. Notably, both the baseline Faradaic efficiency and thermochemical CH_4 conversion were set at 95%, approaching the upper range reported for practical systems. Therefore, the +10% perturbation for these two parameters was capped at 100% to ensure physical consistency.

Table S19. Sensitivity analysis data for key parameters of the representative T-E pathway

Parameters	Perturbation	Value	Energy consumption (kWh m^{-3})	GHG intensity (kg CO_2e m^{-3})	Impact (%)
Baseline (T-E pathway)	-	-	0.6149	0.5087	-
Faradaic efficiency (%)	10% worse	85.5*	0.6555	0.5748	12.99
	10% better	100	0.5966	0.4756	-6.50
Formate credit (kg CO_2e kg^{-1})	10% worse	3.276	0.6149	0.5500	8.11
	10% better	4.004	0.6149	0.4675	-8.11
Grid emission factor (kg CO_2e kWh^{-1})	10% worse	0.591	0.6149	0.5418	6.50
	10% better	0.483	0.6149	0.4758	-6.48
Cell voltage (V)	10% worse	2.75	0.6515	0.5284	3.87
	10% better	2.25	0.5783	0.4891	-3.86
CH_4 Conversion (%)	10% worse	85.5*	0.5864	0.5247	3.15
	10% better	100	0.6299	0.5004	-1.64

*The baseline values for Faradaic efficiency and CH_4 conversion were set at 95%. The +10% perturbation was capped at 100% to ensure physical consistency.

3.2 Regional distribution of GHG performance (Fig.3)

Regional and temporal variations in GHG performance were evaluated using a scenario-based LCA framework. The temporal background inventories used in this study were adapted from Du et al. (2023)[1], who developed province-resolved wastewater-sector GHG scenarios for 2009, 2019, 2030, and 2050. The projected inventories account for concurrent changes in wastewater treatment performance, electricity decarbonization, chemical consumption, and fugitive emissions. Therefore, the temporal scenarios were implemented as integrated background inventories rather than by independently varying a single parameter.

In addition to province-specific grid emission factors, the temporal scenarios (2009, 2019, 2030, and 2050) also incorporated changes in wastewater-related fugitive emissions, electricity structure, chemical consumption, and process energy demand according to the corresponding background inventories and projected decarbonization conditions. Therefore, the differences observed in Fig. 3a-c do not originate from a single parameter, but reflect the combined influence of evolving energy systems, wastewater emission profiles, and process-related inventories under different regional and temporal scenarios (Table S14). To further compare regional disparities, the provinces were grouped into seven geographical regions of China (Northwest, Southwest, North, Northeast, East, Central, and South China) (Figure S2). For each region, the average GHG intensity was calculated from all included provinces under the corresponding temporal scenario (2009, 2019, 2030, and 2050). For example, Northwest China includes Xinjiang, Ningxia, Qinghai, Gansu, and Shaanxi. The bar values shown in Fig. 3e represent the regional mean GHG intensity, while the error bars indicate the inter-provincial standard deviation within each region.

To evaluate the carbon emission reduction equivalent (*CER*) shown in Fig. 3d, the provincial mitigation potential was calculated as:

$$CER = Q_{wwtp} \times max(0, min(Emission_{baseline} - Emission_{total}, Emission_{baseline})) \quad \text{(Eq. S19)}$$

where CER is the carbon emission reduction equivalent (Mt CO_2e yr^{-1}), Q_{wwtp} is the annual wastewater treatment volume of each province (m^3 yr^{-1}), obtained from Table S13, and $Emission_{baseline}$ is the national-average GHG intensity of the conventional WWTP system in 2019 (0.7917 kg CO_2e m^{-3}), $Emission_{total}$ is the total GHG intensity of the evaluated pathway (kg CO_2e m^{-3}). The resulting values were converted from kg CO_2e yr^{-1} to Mt CO_2e yr^{-1} for visualization.

When $Emission_{total}$ <0, the mitigation benefit was capped at the baseline value (corresponding to 100% reduction relative to the conventional WWTP baseline). Conversely, when $Emission_{total}$>$Emission_{baseline}$, the pathway was considered to provide no effective carbon reduction, and the corresponding mitigation value was set to zero.

To evaluate the effect of cross-regional electricity supply on the GHG performance of the T-E pathway in Beijing, the local grid emission factor was replaced with source-specific low-carbon electricity emission factors adjusted for transmission losses (Fig.3f).

The effective emission factor of imported electricity was calculated as:

$$EF_{imported} = EF_{source} \times (1 + \lambda_{loss} \times \frac{D}{1000}) \quad \text{(Eq. S20)}$$

where $EF_{imported}$ is the effective carbon emission factor of imported electricity delivered to Beijing (kg CO_2e kWh^{-1}), EF_{source} is the life-cycle emission factor of the electricity source at the generation side (kg CO_2e kWh^{-1}), D is the transmission distance from the source region to Beijing (km), and λ_{loss} is the transmission loss factor, corresponding to 3.5% per 1000 km, based on reported transmission loss rates in China's power grid[50,51]. This approach was applied to three representative imported electricity scenarios: photovoltaic power from Shandong, offshore wind power from Shanghai, and nuclear power from Guangdong. The resulting $EF_{imported}$ values were then substituted for the Beijing grid emission factor in Equation (3), while all other process parameters were kept unchanged. The updated values were used to recalculate the overall GHG intensity shown in Fig. 3f.

3.3 Performance of T-E pathway across CO_2/CH_4 co-emission scenarios (Fig.4)

To evaluate the applicability of the T-E pathway under broader mixed-emission conditions, nine representative CO_2/CH_4 co-emission sources were considered, including biomass combustion (BC), sludge composting (SC), landfill gas (LF), manure storage (MS), wastewater treatment (WWTP), paddy fields (PF), coke oven gas (COG), coal mine methane (CMM), and ruminant enteric fermentation (RI).

Literature-reported CO_2/CH_4 mass ratios for these sources span a wide range. Biomass combustion and sludge composting generally exhibit CO_2-rich conditions, with reported $\log_{10}$ (CO_2/CH_4 mass ratio) ranges of approximately 1.00~1.50 and 1.18~1.48, respectively, consistent with reported flue-gas and composting emission measurements[54-59]. Landfill gas typically ranges from 0.48-0.70, in agreement with reported landfill methane compositions and IPCC default values[59,60]. Manure storage and wastewater treatment are distributed near balanced conditions, ranging from -0.10~0.10 and -0.15~0.10, respectively, consistent with agricultural emission inventories and municipal wastewater assessments[61-63]. Paddy fields and coke oven gas are relatively CH_4-rich, with reported ranges of -0.70 to -0.52 and -0.78 to -0.60, respectively[64,65]. Coal mine methane and ruminant enteric fermentation represent the most methane-dominant scenarios, with ranges of -1.00 to -0.70 and -1.50 to -1.30, respectively, according to reported coal-mine methane inventories and enteric fermentation measurements[66-68]. These reported ranges are summarized in Fig. 4a using a log10 (CO_2/CH_4 mass ratio) scale.

To represent different co-emission conditions, the relative amounts of CH_4 and CO_2 were adjusted according to the prescribed CO_2/CH_4 mass ratios. Five nominal scenarios (10:1, 5:1, 1:1, 1:5, and 1:10) were constructed to represent CO_2-rich to CH_4-rich emission profiles. The corresponding CH_4 and CO_2 masses were subsequently converted into molar quantities and introduced into the LCA and TEA framework described above.

The CO2/CH4 mass ratio was defined as:

$$R_{CO2/CH4} = \frac{m_{CO2}}{m_{CH4}} \quad \text{(Eq. S21)}$$

where $R_{CO2/CH4}$ is the prescribed CO_2/CH_4 mass ratio (dimensionless), and m_{CO2} and m_{CH4} are the corresponding carbon dioxide and methane masses in the emission stream, respectively.

Table S20. CH_4 and CO_2 inputs under nominal CO_2/ CH_4 co-emission scenarios

	Scenario	CH_4 (kg)	CO_2 (kg)	CH_4 (mol)	CO_2 (mol)
CO_2-rich	10:1	0.0063	0.6327	0.394	14.38
	5:1	0.0072	0.3618	0.451	8.222
Balanced	1:1	0.0081	0.0928	0.507	2.11
	1:5	0.0084	0.0168	0.523	0.382
CH_4-rich	1:10	0.0084	0.0084	0.525	0.191

The resulting CH_4 and CO_2 masses were subsequently converted into molar quantities, as summarized in Table S20, and incorporated into the LCA and TEA framework described above. The calculated gas inventories were used to evaluate the residual GHG intensity ratio of different WtC configurations under each co-emission scenario (Fig. 4b). The subsequent calculations of GHG intensity under fossil-based and low-carbon electricity scenarios (Fig. 4c), as well as the temporal projection from 2019 to 2050 (Fig. 4d), followed the same LCA framework and scenario-based temporal methodology described in Sections 3.1 and 3.2.

3.4 Experiment validation

To further evaluate the physical plausibility of the inventory assumptions and operating parameters adopted in the LCA and TEA framework, representative thermochemical and electrochemical experiments were conducted for the T-E pathway (Figure S3).

The integrated PSE reactor was a laboratory-designed membrane-electrode assembly consisting of a Bi_2O_3-coated gas-diffusion cathode, a Ni foam anode, an anion-exchange membrane (FAA-3-50, Fumatech), a cation-exchange membrane (Nafion 117, DuPont), and a central solid polymer electrolyte layer (PSE layer) positioned between the two ion-exchange membranes. The PSE layer was fabricated from polystyrene and had a thickness of approximately 2.5 mm. CO_2 derived from the thermochemical stage was continuously supplied to the cathode compartment, while deionized water (DI water) was used as the feed solution in the product-collection compartment. A KOH solution was circulated through the anode compartment to maintain ionic conductivity. During operation, formate generated at the cathode was continuously transported and accumulated in the collection compartment, while oxygen was evolved at the anode. The overall reactor configuration is illustrated in Fig. 6g and Fig. S3. Detailed information regarding catalyst specifications, membrane types, suppliers, feed solution properties, and key reactor parameters is summarized in Table S21.

The experimental results show good agreement with the assumptions adopted in the calculation framework (Table S23). For the thermochemical process, CH_4 conversion reached 98 ± 1.5%, close to the assumed conversion efficiency of 95% used in the model.

In the electrochemical step, short-term electrolysis experiments were first conducted to determine the Faradaic efficiency (*FE*) toward formate under controlled conditions. Formate concentrations were quantified by ^{1}H NMR using the calibration curve shown in Fig. S3d. The FE was calculated according to:

$$FE = \frac{C_{exp} \times V \times n \times F}{I \times t} \quad \text{(Eq. S22)}$$

where (C_{exp}) is the experimentally measured formate concentration, (V) is the volume of the product-collection solution (25 mL), (n) is the electron transfer number for formate production (n=2), (F) is the Faraday constant, (I) is the applied current (150 mA), and (t) is the electrolysis time (300 s). Three replicate experiments yielded Faradaic efficiencies toward formate in the range of 96-98%, corresponding to an average value of 97.2 ± 1.2% (Table S22). The measured cell voltage was 2.5 ± 0.3 V, consistent with the operating conditions assumed in the calculation framework.

The experimentally determined *FE* was subsequently used to evaluate the consistency between the theoretical formate accumulation predicted by Faraday's law and the formate concentration measured during long-term PSE reactor operation. Under representative operating conditions, the experimentally obtained formate concentration reached approximately 0.41 mol L^{-1} (Fig. 6i). Using the experimentally determined *FE* value (97.2 ± 1.2%), Faraday's law predicts a theoretical formate concentration of approximately 0.43 mol L^{-1} under the same operating conditions:

$$C = \frac{FE \times I \times t}{V \times n \times F} \times 100\% \quad \text{(Eq. S23)}$$

where (C) is the formate concentration, (FE) is the Faradaic efficiency, (I) is the applied current (100 mA), (t) is the electrolysis time (240 h), (V) is the volume of the product-collection solution (1 L), (n) is the electron transfer number for formate production (n=2), and (F) is the Faraday constant.

The close agreement between the measured and predicted concentrations indicates that the experimentally determined electrochemical performance is consistent with the assumptions adopted in the LCA and TEA framework. A comparison between model assumptions and experimental observations is summarized in Table S23. Together, these results support the physical plausibility of the key parameters adopted in the LCA and TEA analyses.

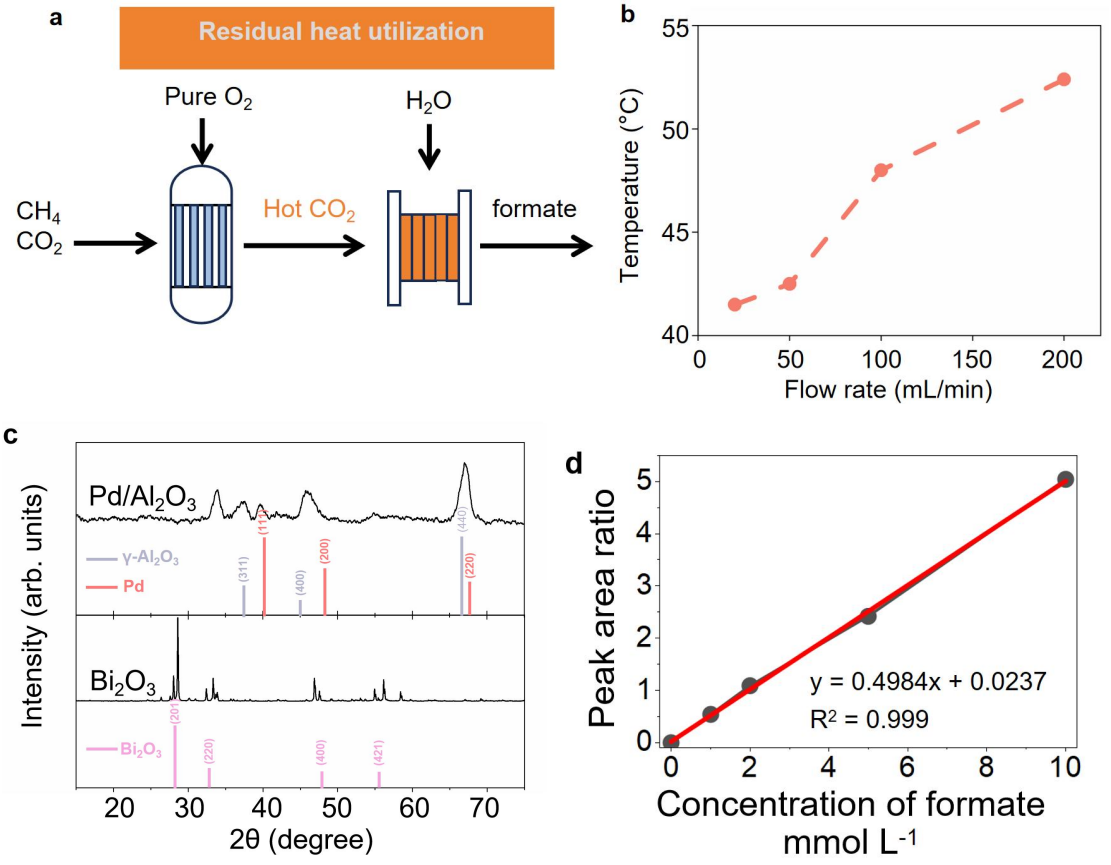

Supplementary Fig. 3. Experimental validation of the thermochemical-electrochemical (T-E) coupling pathway. a, Schematic of the T-E system integrating thermochemical CH_4 oxidation and electrochemical CO_2 reduction. b, Outlet gas temperature as a function of flow rate. c, XRD patterns of Pd/Al_2O_3 and Bi_2O_3 catalysts. d, Calibration curve for formate quantification by ^1H NMR. The peak area ratio exhibited a linear relationship with formate concentration over the investigated concentration range. The regression equation (y = 0.4984x + 0.0237, R^2 = 0.999) was used to determine formate concentrations in electrolysis samples and calculate Faradaic efficiencies.

Table S21. Materials and reactor configuration used in the experimental validation

(a) Materials and key components

Category	Material	Specification	Supplier
Cathode catalyst	Bi_2O_3 catalyst	99.9% purity	SCI Materials Hub
Thermochemical catalyst	Pd/Al_2O_3 catalysts	Pd loading: 0.1, 0.5, and 1 wt%	SCI Materials Hub
AEM	FAA-3-50	Anion-exchange membrane	Fumatech
CEM	Nafion 117	Cation-exchange membrane	DuPont
Feed solution	DI water	Resistivity > 18 MΩ • cm	Laboratory supply
Anolyte	KOH	Analytical grade	SCI Materials Hub

(b) PSE reactor configuration

Parameter	Specification/value
Reactor type	Laboratory-designed PSE reactor
Cathode support	Gas diffusion electrode
Anode material	Ni foam
Cathode geometric area	4 cm^2
Bi_2O_3 loading	1.5 mg cm^{-2}
CO_2 flow rate	40 sccm
PSE layer material	Polystyrene
PSE layer thickness	2.5 mm

Table S22. Replicate Faradaic efficiency measurements for formate production in the integrated PSE reactor

Replicate	Peak area ratio	Formate concentration (mmol L^{-1})	Theoretical formate concentration (mmol L^{-1})	FE (%)
1	4.49	8.961	9.328	96.07
2	4.60	9.182	9.328	98.44
3	4.54	9.062	9.328	97.15
Mean ± SD		9.068±0.111		97.2±1.2

Note: NMR peak area ratios were obtained by integration of the formate signal using Jade software. Formate concentrations were calculated using the calibration curve shown in Fig. S3d. Faradaic efficiencies were calculated according to Eq. S22. Three independent experiments were conducted under identical operating conditions.

Table S23. Comparison of key parameters between model assumptions and experimental validation

Process	Parameter	Model assumption	Experimental value	Consistency
Thermochemical	CH_4 conversion (%)	95	98±1.5	Within expected range
Electrochemical	Cell voltage (V)	2.5	2.5±0.3	Within expected range
Electrochemical	*FE* (%)	95	97.2±1.2	Within expected range
Electrochemical	Formate concentration (mol L^{-1})	0.43*	0.41	Consistent

Note: The *FE* value of 95% was adopted as a conservative model assumption. The theoretical formate concentration (0.43 mol L^{-1}) was calculated according to Eq. S23 using the experimentally determined FE value (97.2 ± 1.2%) and the operating conditions employed in the long-term PSE reactor experiment.

Reference

1 Du, W.-J. *et al.* Spatiotemporal pattern of greenhouse gas emissions in China's wastewater sector and pathways towards carbon neutrality. *Nature Water* **1**, 166-175 (2023).

2 Bauer, F., Hulteberg, C., Persson, T. & Tamm, D. Biogas upgrading - Review of commercial technologies. (2013).

3 He, X. & Hägg, M.-B. Energy Efficient Process for CO2 Capture from Flue gas with Novel Fixed-site-carrier Membranes. *Energy Procedia* **63** (2014). https://doi.org:10.1016/j.egypro.2014.11.018

4 Jouny, M., Luc, W. & Jiao, F. General Techno-Economic Analysis of CO2 Electrolysis Systems. *Industrial & Engineering Chemistry Research* **57**, 2165-2177 (2018). https://doi.org:10.1021/acs.iecr.7b03514

5 Kondratenko, E. V., Mul, G., Baltrusaitis, J., Larrazábal, G. O. & Pérez-Ramírez, J. Status and perspectives of CO2 conversion into fuels and chemicals by catalytic, photocatalytic and electrocatalytic processes. *Energy & Environmental Science* **6**, 3112-3135 (2013). https://doi.org:10.1039/C3EE41272E

6 Olah, G., Goeppert, A. & Prakash, S. Chemical Recycling of Carbon Dioxide to Methanol and Dimethyl Ether: From Greenhouse Gas to Renewable, Environmentally Carbon Neutral Fuels and Synthetic Hydrocarbons. *The Journal of organic chemistry* **74**, 487-498 (2009). https://doi.org:10.1021/jo801260f

7 Schwach, P., Pan, X. & Bao, X. Direct Conversion of Methane to Value-Added Chemicals over Heterogeneous Catalysts: Challenges and Prospects. *Chemical reviews* **117** (2017). https://doi.org:10.1021/acs.chemrev.6b00715

8 Metcalf, Eddy, I. & Aecom. *Wastewater engineering: Treatment and resource recovery*. 5 edn, (McGraw-Hill Education, 2014).

9 Tchobanoglous, G., Burton, F. L. & Stensel, H. D. *Wastewater engineering: Treatment and reuse*. 4 edn, (McGraw-Hill, 2003).

10 Yang, Z. *et al.* MOF derived bimetallic CuBi catalysts with ultra-wide potential window for high-efficient electrochemical reduction of CO2 to formate. *Applied Catalysis B: Environmental* **298**, 120571 (2021). https://doi.org:https://doi.org/10.1016/j.apcatb.2021.120571

11 Xiong, Y. *et al.* Rapid synthesis of amorphous bimetallic copper-bismuth electrocatalysts for efficient electrochemical CO2 reduction to formate in a wide potential window. *Journal of CO2 Utilization* **51**, 101621 (2021). https://doi.org:https://doi.org/10.1016/j.jcou.2021.101621

12 Wang, J. *et al.* In-Sn alloy core-shell nanoparticles: In-doped SnOx shell enables high stability and activity towards selective formate production from electrochemical reduction of CO2. *Applied Catalysis B: Environmental* **288**, 119979 (2021). https://doi.org:https://doi.org/10.1016/j.apcatb.2021.119979

13 Ning, S. *et al.* Electrochemical reduction of SnO2 to Sn from the Bottom: In-Situ formation of SnO2/Sn heterostructure for highly efficient

electrochemical reduction of carbon dioxide to formate. *Journal of Catalysis* **399**, 67-74 (2021). https://doi.org:https://doi.org/10.1016/j.jcat.2021.04.028

14 Zhao, M. *et al.* Atom vacancies induced electron-rich surface of ultrathin Bi nanosheet for efficient electrochemical CO2 reduction. *Applied Catalysis B: Environmental* **266**, 118625 (2020). https://doi.org:https://doi.org/10.1016/j.apcatb.2020.118625

15 Zha, B., Li, C. & Li, J. Efficient electrochemical reduction of CO2 into formate and acetate in polyoxometalate catholyte with indium catalyst. *Journal of Catalysis* **382**, 69-76 (2020). https://doi.org:https://doi.org/10.1016/j.jcat.2019.12.010

16 Wu, D., Chen, W., Wang, X., Fu, X.-Z. & Luo, J.-L. Metal-support interaction enhanced electrochemical reduction of CO2 to formate between graphene and Bi nanoparticles. *Journal of CO2 Utilization* **37**, 353-359 (2020). https://doi.org:https://doi.org/10.1016/j.jcou.2020.02.007

17 Qian, Y., Liu, Y., Tang, H. & Lin, B.-L. Highly efficient electroreduction of CO2 to formate by nanorod@2D nanosheets SnO. *Journal of CO2 Utilization* **42**, 101287 (2020). https://doi.org:https://doi.org/10.1016/j.jcou.2020.101287

18 Jiang, X. *et al.* A highly selective tin-copper bimetallic electrocatalyst for the electrochemical reduction of aqueous CO2 to formate. *Applied Catalysis B: Environmental* **259**, 118040 (2019). https://doi.org:https://doi.org/10.1016/j.apcatb.2019.118040

19 Zhu, X. *et al.* Electrochemical reduction of carbon dioxide on copper-based nanocatalysts using the rotating ring-disc electrode. *Electrochimica Acta* **283**, 1037-1044 (2018). https://doi.org:https://doi.org/10.1016/j.electacta.2018.07.025

20 Li, P. *et al.* In situ dual doping for constructing efficient CO2-to-methanol electrocatalysts. *Nature communications* **13**, 1965 (2022).

21 Yang, H. *et al.* Scalable production of efficient single-atom copper decorated carbon membranes for CO2 electroreduction to methanol. *Journal of the American Chemical Society* **141**, 12717-12723 (2019).

22 Yang, D. *et al.* Selective electroreduction of carbon dioxide to methanol on copper selenide nanocatalysts. *Nature Communications* **10**, 677 (2019).

23 Mou, S. *et al.* Boron phosphide nanoparticles: a nonmetal catalyst for high-selectivity electrochemical reduction of CO2 to CH3OH. *Advanced Materials* **31**, 1903499 (2019).

24 Zhang, W. *et al.* Electrochemical reduction of carbon dioxide to methanol on hierarchical Pd/SnO2 nanosheets with abundant Pd–O–Sn interfaces. *Angewandte Chemie International Edition* **57**, 9475-9479 (2018).

25 Lu, L. *et al.* Highly efficient electroreduction of CO2 to methanol on palladium–copper bimetallic aerogels. *Angewandte Chemie* **130**, 14345-14349 (2018).

26 Huang, J., Hu, Q., Guo, X., Zeng, Q. & Wang, L. Rethinking Co (CO 3) 0.5 (OH)· 0.11 H 2 O: a new property for highly selective electrochemical

reduction of carbon dioxide to methanol in aqueous solution. *Green Chemistry* **20**, 2967-2972 (2018).

27 Huang, J., Guo, X., Yue, G., Hu, Q. & Wang, L. Boosting CH3OH production in electrocatalytic CO2 reduction over partially oxidized 5 nm cobalt nanoparticles dispersed on single-layer nitrogen-doped graphene. *ACS Applied Materials & Interfaces* **10**, 44403-44414 (2018).

28 Yang, H.-P., Qin, S., Wang, H. & Lu, J.-X. Organically doped palladium: a highly efficient catalyst for electroreduction of CO 2 to methanol. *Green Chemistry* **17**, 5144-5148 (2015).

29 Albo, J., Sáez, A., Solla-Gullón, J., Montiel, V. & Irabien, A. Production of methanol from CO2 electroreduction at Cu2O and Cu2O/ZnO-based electrodes in aqueous solution. *Applied Catalysis B: Environmental* **176**, 709-717 (2015).

30 Qiu, X.-F. *et al.* A Stable and Conductive Covalent Organic Framework with Isolated Active Sites for Highly Selective Electroreduction of Carbon Dioxide to Acetate. *Angewandte Chemie International Edition* **61**, e202206470 (2022). https://doi.org:https://doi.org/10.1002/anie.202206470

31 De, R. *et al.* Electrocatalytic Reduction of CO2 to Acetic Acid by a Molecular Manganese Corrole Complex. *Angewandte Chemie International Edition* **59**, 10527-10534 (2020). https://doi.org:https://doi.org/10.1002/anie.202000601

32 Wang, Y. *et al.* CO2 reduction to acetate in mixtures of ultrasmall (Cu)n,(Ag)m bimetallic nanoparticles. *Proceedings of the National Academy of Sciences* **115**, 278-283 (2018). https://doi.org:10.1073/pnas.1713962115

33 Kim, T. *et al.* Enhancing C2–C3 Production from CO2 on Copper Electrocatalysts via a Potential-Dependent Mesostructure. *ACS Applied Energy Materials* **1**, 1965-1972 (2018). https://doi.org:10.1021/acsaem.8b00048

34 Genovese, C., Ampelli, C., Perathoner, S. & Centi, G. Mechanism of C–C bond formation in the electrocatalytic reduction of CO2 to acetic acid. A challenging reaction to use renewable energy with chemistry. *Green Chemistry* **19**, 2406-2415 (2017). https://doi.org:10.1039/C6GC03422E

35 Liu, Y., Chen, S., Quan, X. & Yu, H. Efficient Electrochemical Reduction of Carbon Dioxide to Acetate on Nitrogen-Doped Nanodiamond. *Journal of the American Chemical Society* **137**, 11631-11636 (2015). https://doi.org:10.1021/jacs.5b02975

36 Wang, P. *et al.* Boosting electrocatalytic CO2–to–ethanol production via asymmetric C–C coupling. *Nature Communications* **13**, 3754 (2022). https://doi.org:10.1038/s41467-022-31427-9

37 Xu, H. *et al.* Highly selective electrocatalytic CO2 reduction to ethanol by metallic clusters dynamically formed from atomically dispersed copper. *Nature Energy* **5**, 623-632 (2020). https://doi.org:10.1038/s41560-020-0666-x

38 Karapinar, D. *et al.* Electroreduction of CO2 on Single-Site Copper-Nitrogen-Doped Carbon Material: Selective Formation of Ethanol and Reversible Restructuration of the Metal Sites. *Angewandte Chemie*

International Edition **58**, 15098-15103 (2019). https://doi.org:https://doi.org/10.1002/anie.201907994

39 Prajapati, A., Sartape, R., Kani, N. C., Gauthier, J. A. & Singh, M. R. Chloride-Promoted High-Rate Ambient Electrooxidation of Methane to Methanol on Patterned Cu–Ti Bimetallic Oxides. *ACS Catalysis* **12**, 14321-14329 (2022). https://doi.org:10.1021/acscatal.2c03619

40 Tian, H. *et al.* Selective electrooxidation of methane to formic acid by atomically dispersed CuOx and its induced Lewis acid sites on V2O5 in a tubular electrode. *Applied Catalysis B: Environment and Energy* **351**, 124001 (2024). https://doi.org:https://doi.org/10.1016/j.apcatb.2024.124001

41 Jiang, H. *et al.* Electrocatalytic methane direct conversion to methanol in electrolyte of ionic liquid. *Electrochimica Acta* **445**, 142065 (2023). https://doi.org:https://doi.org/10.1016/j.electacta.2023.142065

42 Wang, Q. *et al.* Electrocatalytic Methane Oxidation Greatly Promoted by Chlorine Intermediates. *Angewandte Chemie International Edition* **60**, 17398-17403 (2021). https://doi.org:https://doi.org/10.1002/anie.202105523

43 Xu, N. *et al.* Electro-conversion of methane to alcohols on "capsule-like" binary metal oxide catalysts. *Applied Catalysis B: Environmental* **282**, 119572 (2021). https://doi.org:https://doi.org/10.1016/j.apcatb.2020.119572

44 Wernet, G. *et al.* The ecoinvent database version 3 (part I): overview and methodology. *The International Journal of Life Cycle Assessment* **21**, 1218-1230 (2016). https://doi.org:10.1007/s11367-016-1087-8

45 Intergovernmental Panel on Climate, C. Climate Change 2023: Synthesis Report. (Intergovernmental Panel on Climate Change, Geneva, Switzerland, 2023).

46 China City Greenhouse Gas Working, G. China Products Carbon Footprint Factors Database. (2025).

47 National, D. & Reform, C. Notice on Improving the Pricing Mechanism for Wastewater Treatment and Resource Recovery. (National Development and Reform Commission of China, Beijing, China, 2021).

48 Sci. Chemical Market Price Database. (2024).

49 Peters, M. S., Timmerhaus, K. D. & West, R. E. *Plant Design and Economics for Chemical Engineers*. 5 edn, (McGraw-Hill, 2003).

50 National Bureau of Statistics of, C. *China Energy Statistical Yearbook*. (China Statistics Press, 2023).

51 State Grid Corporation of, C. *Development report of China's power grid*. (China Electric Power Press, 2021).

52 World, B. State and Trends of Carbon Pricing 2023. (World Bank, Washington, DC, 2023).

53 Zeng, S. The influencing factors of the carbon trading price. *Sustainability* **15**, 2203 (2023).

54 Nordahl, S. L., Preble, C. V., Kirchstetter, T. W. & Scown, C. D. Greenhouse gas and air pollutant emissions from composting. *Environmental science & technology* **57**, 2235-2247 (2023).

55 Agency, U. S. E. P. Inventory of U.S. Greenhouse Gas Emissions and Sinks: 1990–2022. Chapter 7: Waste. (U.S. Environmental Protection Agency (EPA), Washington, D.C., 2024).
56 Akagi, S. K. Emission factors for open and domestic biomass burning. *Atmospheric Chemistry and Physics* **11**, 4039-4072 (2011).
57 Andreae, M. O. & Merlet, P. Emission of trace gases and aerosols from biomass burning. *Global Biogeochemical Cycles* **15**, 955-966 (2001).
58 Hao, X., Chang, C. & Larney, F. J. Carbon, nitrogen balances and greenhouse gas emission during cattle feedlot manure composting. *Journal of Environmental Quality* **33**, 37-44 (2004).
59 Ipcc. 2006 IPCC Guidelines for National Greenhouse Gas Inventories. (2006).
60 Bogner, J. Mitigation of global greenhouse gas emissions from waste. *Waste Management & Research* **26**, 11-32 (2008).
61 Amon, B. Methane, nitrous oxide and ammonia emissions during storage and after application of dairy cattle slurry. *Agriculture, Ecosystems & Environment* **112**, 153-162 (2006).
62 Ipcc. 2019 Refinement to the 2006 IPCC Guidelines. (2019).
63 Montes, F. Mitigation of methane and nitrous oxide emissions from animal operations. *Journal of Animal Science* **91**, 5070-5094 (2013).
64 Conrad, R. in *Advances in Agronomy* Vol. 96 1-63 (Academic Press, 2007).
65 Saunois, M. The Global Methane Budget 2000-2017. *Earth System Science Data* **12**, 1561-1623 (2020).
66 Gerber, P. J. *Tackling Climate Change Through Livestock*. (FAO, 2013).
67 Karacan, C. Ö. Coal mine methane: A review of capture and utilization practices. *International Journal of Coal Geology* **86**, 121-156 (2011).
68 Knapp, J. R. Invited review: Enteric methane in dairy cattle production. *Journal of Dairy Science* **97**, 3231-3261 (2014).